Braz J Phys (2012) 42:347–354
DOI 10.1007/s13538-012-0097-7

CONDENSED MATTER

Control of Crystallization Kinetics and Study of the Thermal, Structural and Morphological Properties of an $Li_2O–B_2O_3–Al_2O_3$ Vitreous System

Noelio O. Dantas · Valdeir A. Silva · Omar. O. D. Neto · Marcio L. F. Nascimento

Received: 10 April 2012 / Published online: 5 October 2012
© Sociedade Brasileira de Física 2012

Abstract A glass matrix with nominal composition $50Li_2O·45B_2O_3·5Al_2O_3$ (mol%) was synthesized, and its physical properties were investigated by differential thermal analysis (DTA), X-ray diffraction (XRD), and atomic force microscopy (AFM). The glass transition temperature T_g, the crystallization-onset temperature $T_{x,}$, the crystallization peak temperatures T_{c1} and $T_{c2,}$ and the fusion peak temperatures T_{m1} and T_{m2} were determined from at least two glass matrix phases to be approximately 382, 457, 486, 574, 761, and 787 °C, respectively, at 5 °C/min heating rate. Heat treatments at 450 °C for an increasing sequence of time intervals allowed control over the amount of crystallization. Additional information on the crystallization kinetics for the LBA glass matrix was gathered from AFM images, DTA thermograms, and XRD diffractograms. The latter technique showed that $LiBO_2$ (ICDD-16568) and $Li_3AlB_2O_6$ (ICDD-51754) phases are formed in the glass–ceramic system. Debye–Scherrer analysis of the XRD peaks revealed a competition between the evolutions of crystal phases during heat treatment. Activation energies for crystallization, obtained from theoretical models applied to the DTA data showed that the crystallization is heterogeneous. The AFM images demonstrated that this heterogeneous crystallization starts at the surface of the LBA glass matrix and identified crystal sizes in agreement with the results of the Debye–Scherrer analysis. Our study shows that thermal and structural characterization techniques can be combined with theoretical results drawn from well-tested models to offer a unified view of crystallization in a glass–ceramics system.

Keywords Glass · Crystallization · DTA · LBA glass

N. O. Dantas (✉) · V. A. Silva
Laboratório de Novos Materiais Isolantes e Semicondutores (LNMIS),
Instituto de Física, Universidade Federal de Uberlândia,
CP 593,
CEP 38400-902 Uberlândia, MG, Brazil
e-mail: noelio@ufu.br

O. O. D. Neto
Grupo de Óptica e Informação Quântica (GOIQ),
Instituto de Física, Universidade Federal de Uberlândia,
CP 593,
CEP 38400-902 Uberlândia, MG, Brazil

M. L. F. Nascimento
Vitreous Materials Laboratory, Institute of Humanities,
Arts and Sciences, Federal University of Bahia,
Rua Barão de Jeremoabo s/n, Idioms Center Pavilion (PAF IV),
Ondina University Campus,
40170-115 Salvador, Bahia, Brazil

M. L. F. Nascimento
PROTEC/PEI—Postgraduate Program in Industrial Engineering,
Department of Chemical Engineering, Polytechnic School,
Federal University of Bahia,
Rua Aristides Novis 2, Federação,
40210-630 Salvador, Bahia, Brazil

1 Introduction

The crystallization of glasses involves numerous crystallites that are independently nucleated and simultaneously grown [1]. In glasses devoid of nucleating agents, internal nucleation is oftentimes observed, although surface crystallization is the rule [2]. To distinguish one process from the other and to provide information on the dynamics of nucleation and growth, systematic measurements of the surface or volume fraction of the transformed material prove instrumental since they monitor the evolution of the process and yield data that can be interpreted in the light of the JMAYK theory, the comprehensive description of the kinetics of crystallization under isothermal conditions independently developed by Kolmogorov [3], Johnson and Mehl [4],

Avrami [5–7], and Yerofyeyev [8] in the late 1930s to 1940s.

The impact of crystallization on technological applications has motivated intense scientific activity aimed at understanding and controlling glass-crystallization kinetics. The list of examples includes the search for glass–ceramic scintillators [9, 10] and dosimeters [11], and the study, in conjunction with crystal-field theories, of the optical properties of rare earth ions embedded in glass–ceramic compositions [12, 13]. Borate glasses, in particular, have received wide attention [14–17]. Compositional modifications affecting their physical properties have been investigated. Of special importance are the addition of Li^+ ions, which favors crystallization while incrementing the capacity to store transition-metal ions, and the insertion of Al_2O_3, which enhances the chemical durability and therefore broadens the range of technological benefits [18, 19].

Attentive to the significance of such benefits, we have investigated the kinetics of crystallization in a lithium–borate–aluminate (LBA) glass. Our study combines a number of experimental procedures: differential thermal analysis (DTA), X-ray diffraction (XRD), and atomic force microscopy (AFM), which probed the thermal, structural and morphological properties of the material, respectively. The results provide a unified view of crystallization in the matrix, allowing control over the amount of crystallization, identifying activation energies, showing competition between crystal phases and demonstrating that the crystallites are nucleated at the surface.

2 Experimental Method

An LBA glass matrix with nominal composition $50Li_2O{\cdot}45B_2O_3{\cdot}5Al_2O_3$ (mol%) was synthesized by fusion at 1,000 °C for 10 min in porcelain crucibles in ambient atmosphere. The resulting flux was splat cooled and compressed into two 2-mm-thick brass plates previously cooled to 0 °C. After the vitreous samples were pulverized, grain sizes smaller than or equal to 53 μm were selected for DTA and XRD. The LBA glass matrix plates were optically polished for AFM imaging.

The samples were thermally characterized in alumina crucibles under nitrogen atmosphere in a Shimadzu DTA-50, with heating rates ranging from 5 to 25 °C/min. The characteristic temperatures were determined by the *tangent method*, which consists of drawing base lines to the left and to the right of each event in the DTA thermogram and determining the temperature at which the extensions of these base lines intersect. The results dictated the temperature (450 °C) at which both the powder and the plate LBA glass matrix samples were thermally treated, for intervals ranging from 1 to 7 h.

Following each thermal treatment, a DTA thermogram, an XRD diffractogram, and an AFM image of the resulting glass–ceramic sample were taken, the last one with a Shimadzu SPM-9600 in the dynamic mode. The X-ray diffractograms were obtained with a Shimadzu XRD-6000 set at a $CuK_{\alpha 1}$ wavelength of $\lambda = 1.54$ A.

3 Results and Discussion

Figure 1a shows the thermogram of the lithium-carbonate (Li_2CO_3), boron-oxide (B_2O_3) and alumina (Al_2O_3) reagent mixture that produced the $50Li_2O{\cdot}45B_2O_3{\cdot}5Al_2O_3$ (mol%) composition, before heating. More specifically, the plot describes the thermal behavior of the composition while heated at 5 °C/min throughout the sintering of the powder, before being melted to produce the glass material in our study. Different stages can be identified in the heating cycle, identified by capital letters along the plot. A substantial amount of water is lost in range *A*, from 100C to 180 °C. From *B* to *E* (from 450 to 680 °C), decomposition and partial melting of the reactants yields the final, above-described composition. The particles in the powder are simultaneously sintered, and water is continuously lost in these processes, which start near the melting temperature of trigonal B_2O_3 (450 °C). Peak *F*, which signals the melting of the chemical composition, set the temperature (1,000 °C) of the electric furnace used in the synthesis.

Figure 1b shows the thermogram of the LBA glass matrix (vitreous material) at the same heating rate and identifies the temperatures T_g (the glass transition, at approximately 382 °C),

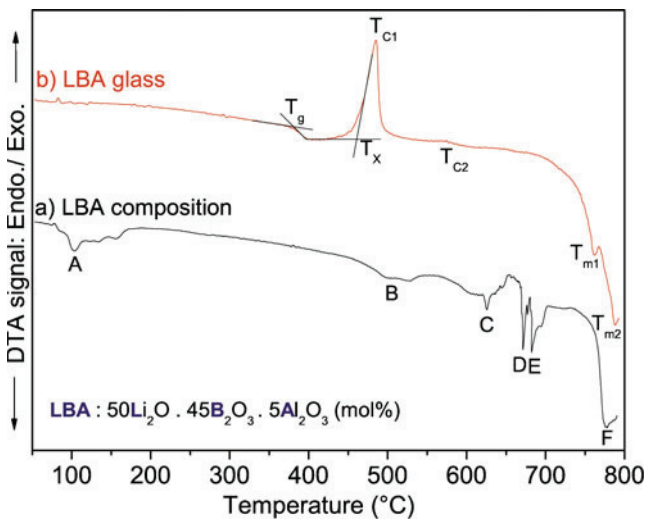

Fig. 1 (*Color online*) LBA glass matrix thermograms at 5 °C/min heating rate. **a** Thermogram of the reactants, before thermal treatment. The labels ***a–f*** indicate thermal ranges of special interest, discussed in the text. **b** Thermogram of the glass matrix. The straight lines define the *tangent method*, which determines the characteristic temperatures

T_{c1} (first-crystallization peak, approximately 486 °C), T_{c2} (second-crystallization peak, approximately 574 °C) and at least two endothermic processes: T_{m1} (approximately 761 °C) and T_{m2} (approximately 787 °C), in which the crystalline phases formed during the first and second crystallizations are decomposed. The characteristic temperatures are collected in Table 1.

To calculate T_g, T_x, and T_c, we extrapolated the heating rate to β=0 °C/min, a procedure recently adopted by Ferreira et al. [20] , to calculate T_{ml} , and by Pedersen et al. [21], to calculate the crystallization-onset temperature T_x. The top row in Table 2 lists the resulting rate-independent characteristic temperatures.

Figure 2a and b shows the thermograms and diffractograms, respectively, of the glass matrix and glass–ceramics samples, treated at 450 °C, for different heat-treatment intervals. The evolution of the two sets of plots as the duration rises from 0 (bottom curves) to 7 h (top curves) shows that, as expected, heat treatment favors crystallization. As the treatment time rises, the areas under the DTA crystallization peaks in Fig. 2a, which are proportional to the glassy volumes remaining in the sample after thermal treatment, are progressively reduced, while the diffraction peaks in Fig. 2b, which measure the crystalline order after treatment, become more salient.

The XRD patterns also identify the crystalline phases in the samples. Several of the peaks are characteristic of the ternary LBA system [22]. The top panel in Fig. 2b assigns the most prominent peaks to the $LiBO_2$ (ICDD-16568) and $Li_3AlB_2O_6$ (ICDD-51754) phases. Additional peaks in the diffractogram indicate that at least one more phase is present, which we were unable to label. The endothermic T_{m1} peaks in Fig. 2a indicate that the $Li_3AlB_2O_6$ phase decomposes into Li_2AlBO_4 and $LiBO_2$, and the T_{m2} peaks indicate that Li_2AlBO_4 turns into $LiBO_2$, a decomposition that has already been identified in the liquid phase [23].

The plots in Fig. 2 show that heat treatment at 450 °C allows fine-tuned control of crystallization. The temperature T_x=450 °C defines the onset of crystallization [20], i.e., it defines growth rates that are small at the macroscopic scale because the thermal energy is just sufficient to overcome the barriers preventing crystallization.

To study the competition among the three major phases associated with the diffraction peaks in Fig. 2b, we obtained

Table 1 Characteristic temperatures of the LBA system (°C) measured at 5 °C/min heating rate

LBA powder					
A	*B*	*C*	*D*	*E*	*F*
100	450	625	671	682	774
LBA Glass					
T_g	T_x	T_{c1}	T_{c2}	T_{m1}	T_{m2}
382	457	486	574	761	787

Table 2 Characteristic temperatures T_g, T_x, and T_{c1} and the Avrami index *n* for the LBA matrix measured at heating rates β ranging from 5 to 25 °C/min

β (°C/min)	T_g (°C)	T_x (°C)	T_{c1} (°C)	*n*
0	380	450	479	–
5	382	457	486	5.5
10	385	466	498	6.6
15	387	479	509	7.1
20	389	485	516	7.3
25	391	490	524	7.5

The first row shows the static limits resulting from the extrapolations of the three temperatures to β=0

the average crystal size $d_{crystal}$ from the Debye–Scherrer equation [24]:

$$d_{crystal} = \frac{0.9\lambda}{(\varphi_2 - \varphi_1)\cos\left(\frac{\varphi_2+\varphi_1}{2}\right)}, \quad (1)$$

where λ is the X-ray wavelength, φ=2θ is the Bragg angle, and φ_1 and φ_2 are the diffraction angles at half maximum of the diffraction peak, so that the first term within parentheses in the denominator at the right-hand side is the full-width at half maximum.

Figure 3 shows the crystal sizes listed in Table 3, extracted from three diffraction peaks, as functions of the treatment time. The open circles (○) belong to a phase growing so fast that a diffraction peak emerges already after 1 h of heat treatment. After 2 h, the peaks associated with the other two crystal phases become visible, which are represented by stars (*) and crosses (+). The plots show that the crystals in the latter two phases grow, while the crystals in the first phase shrink, an indication that the phases represented by the stars and crosses expand at the expense of the phase depicted by the open circles. The error bars (not shown) associated with the crosses are relatively large, because shoulders or secondary peaks next to the diffraction lines degrade our estimates of the parameters on the right-hand side of Eq. (1). This limitation notwithstanding, the trend in Fig. 3 clearly indicates that thermal treatment favors growth of the crystallites labeled by the cross.

Figure 4 shows the DTA curves for heating rates ranging from 5 to 25 °C/min for the LBA glass matrix, i.e., for samples not previously thermally treated. While more detailed information can be extracted at low rates, as indicated by the blown-up plots in Fig. 4b, the crystallization temperature can be determined more accurately at the higher heating rates. The area $\int_{T_i}^{T_f} TdT$ under each crystallization peak is related to the enthalpy change ΔH by the following expression, first proposed

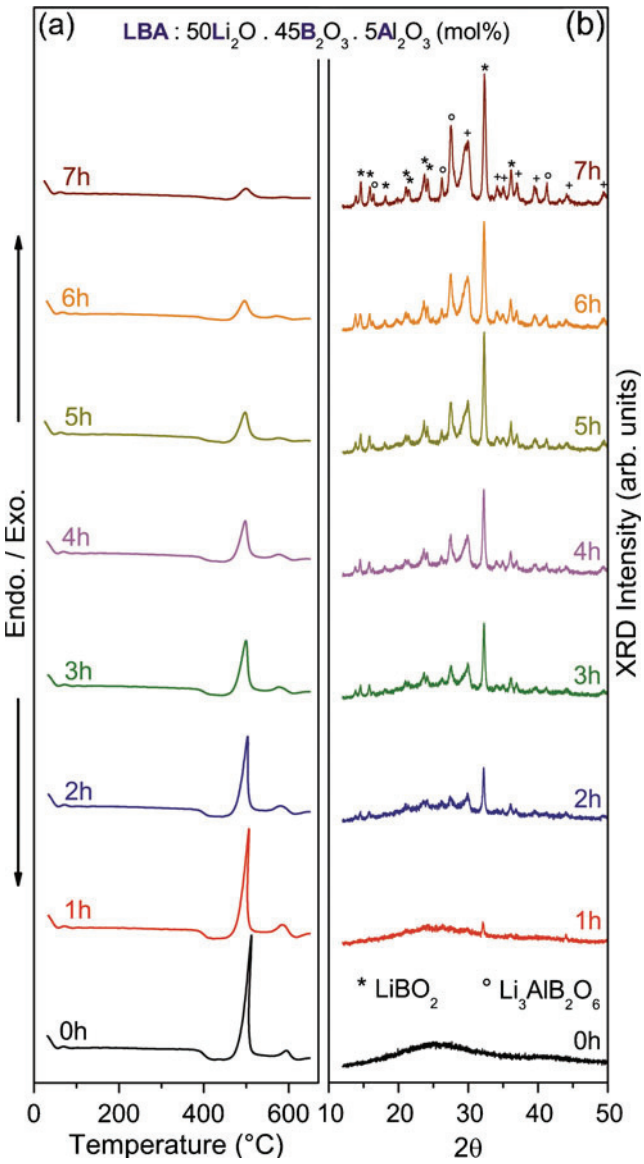

Fig. 2 (*Color online*) **a** Thermograms (DTA) of the LBA glass matrix after heat treatment at 450 °C for the indicated time periods. The area under each prominent peak is proportional to glassy volume remaining in the sample after the heat treatment. **b** Corresponding diffractograms (XRD) of the heat-treated matrix. The stars (*) identify the $LiBO_2$ (ICDD-16568) phase, the open circles (°), the $Li_3AlB_2O_6$ (ICDD-51754) phase, and the crosses (+), a third, undetermined crystal phase

by Kerr and Kulp [25]:

$$\frac{m\,\Delta H}{pq} = \int_{T_i}^{T_f} \Delta T dT, \tag{2}$$

where m is the sample mass, ΔT is the temperature, measured from the base line of the thermogram, T_i and T_f are the initial and final temperatures of the event, p is a dimensionless geometrical factor, and q is the ratio between the thermal conductivity and the heating rate. Since ΔH, the thermal conductivity, and the geometrical factor p are independent of

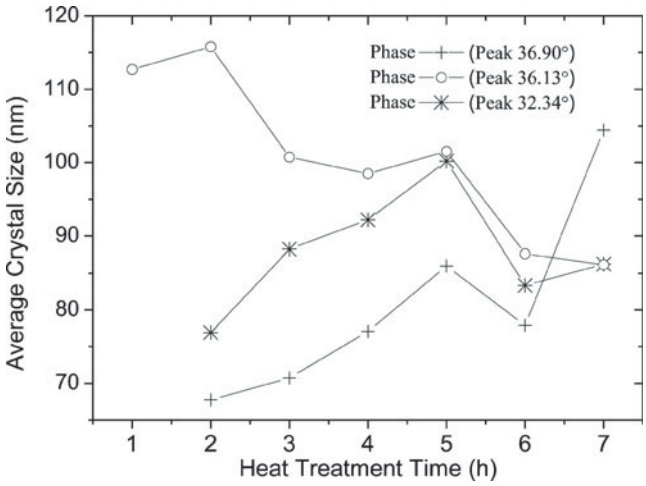

Fig. 3 Average nanocrystal sizes as functions of thermal treatment time for the three phases identified in Fig. 2b, depicted by the same symbols. The straight lines are guides to the eyes. The crystallites in the phases represented by stars (*) and crosses (+) grow at the expense of those in the phase represented by open circles (°)

sample size and heating rate, the left-hand side of Eq. (2) is proportional to the product of the mass m by the heating rate β. Figure 5 shows the area under the peaks in Fig. 4a as a function of $m\beta$. The data points (filled squares) are well fitted by the straight line representing Eq. (2).

From the plots in Fig. 4a we determined the characteristic temperature T_{c1} as a function of the heating rate. From the plot of $\ln(T_{c1}{}^2/\beta)$ as a function of $1/T_{c1}$ in Fig. 5a and the Kissinger expression [26]:

$$\ln\left(\frac{T_{c1}^2}{\beta}\right) = \frac{E_A}{RT_{c1}} + constant, \tag{3}$$

where β is the heating rate and R is the universal gas constant, linear regression yielded the activation enthalpy E_A=(210±18)kJ/mol. Finally, the Avrami parameter n,

Table 3 Average nanocrystal sizes calculated from the widths of the indicated diffraction peaks (shown in Fig. 2b) with the Debye–Scherrer expression [Eq. (1)]

Heat treatment time (h)	* phase (nm) (32.34º peak)	º phase (nm) (36.13º peak)	+ phase (nm) (36.90 peak)
1	–	112.72	–
2	76.91	115.78	67.73
3	88.22	100.77	70.72
4	92.21	98.507	77.08
5	100.21	101.53	85.98
6	83.34	87.61	77.90
7	86.24	86.14	104.42

As in Fig. 2b and 3, a star (*), an open circle (°), and a cross (+) identify the $LiBO_2$ (ICDD-16568) crystalline structure, the $Li_3AlB_2O_6$ (ICDD-51754) structure, and an unknown phase, respectively

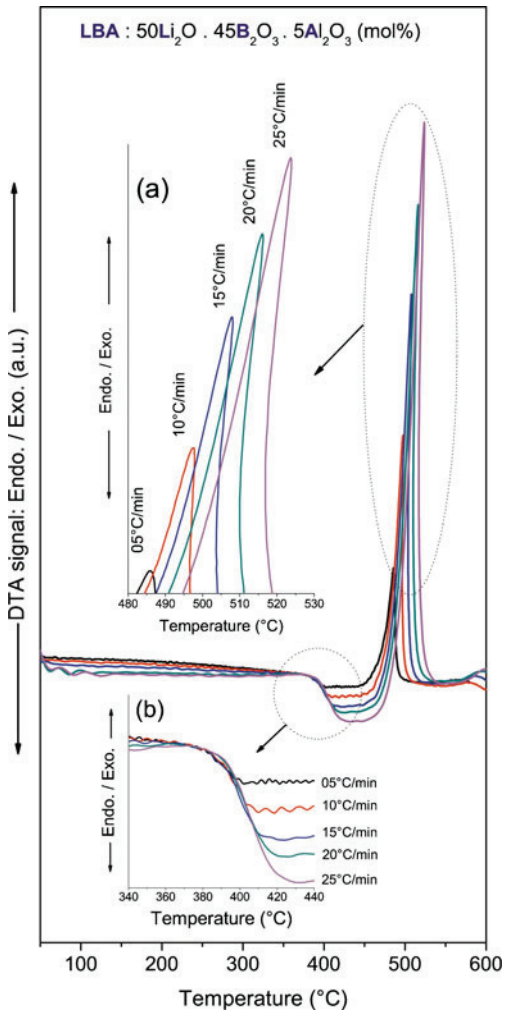

Fig. 4 (*Color online*) Thermograms (DTA) of the vitreous composition for the indicated heating rates. The insets (*b*) and (*a*) show the regions around the glass transition and the first-crystallization peak, respectively, in more detail

which determines the order of the reaction kinetics, was computed from the equality

$$n = \frac{2.5RT_{c1}^2}{E_A\,\Delta^* T}, \tag{4}$$

where $\Delta^* T$ is the width of the crystallization peak at half maximum.

The rightmost column in Table 2 shows that n depends on the heating rate. Albeit compatible with the uncertainties indicated by the error bars in Fig. 6a, the variation points to a nonuniform distribution of activation energies, as a consequence of which different nuclei are formed at different heating rates. To investigate this finding in more detail we might have employed isothermal microscopy, a technique that determines the characteristic temperatures maximizing crystal nucleation and growth [1]. Non-isothermal methods are nonetheless preferable, because they yield equally

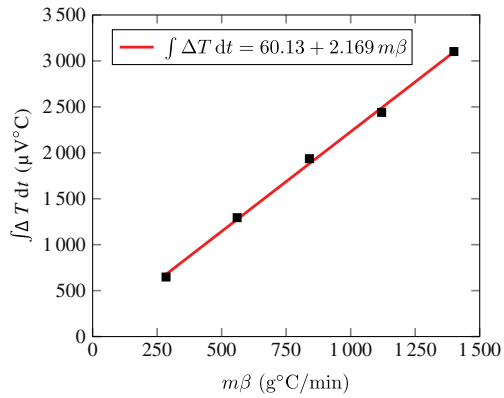

Fig. 5 (*Color online*) Area under crystallization peak as a function of the product of the sample mass m by the heating rate β. The filled squares are the areas from Fig. 4a, while the straight line representing Eq. (2) (slope 2.169±0.053) was obtained by linear regression

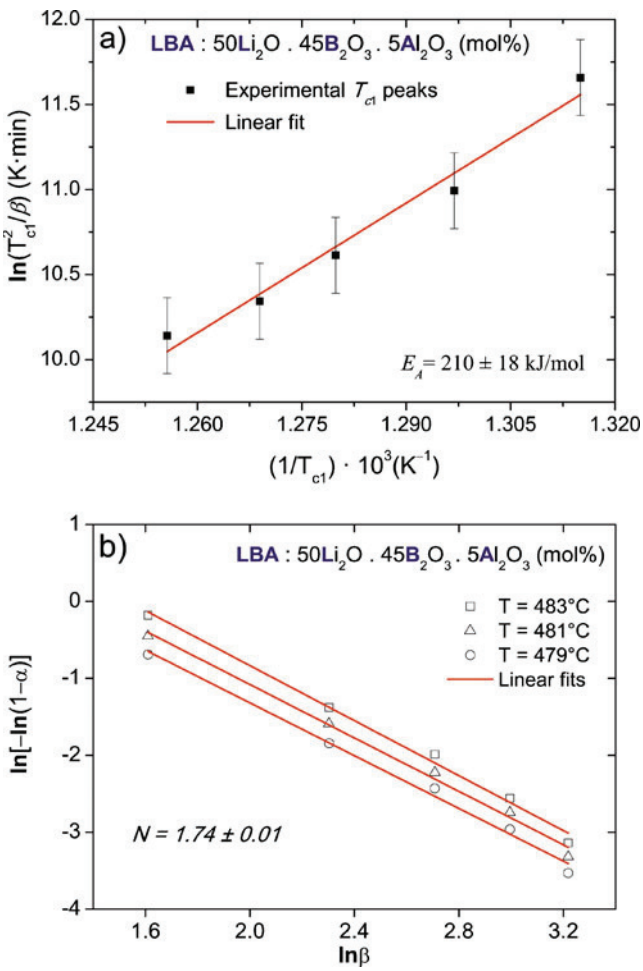

Fig. 6 (*Color online*) **a** Left-hand side of the Kissinger equation [Eq. (3)] as a function of the inverse first-crystallization temperature. The *straight line* depicts the result of linear regression, the slope of which yields the activation energy for crystallization. **b** Left-hand side of the Ozawa equation [Eq. (6)] as functions of the heating rate at the indicated temperatures. The slopes of the linear fits determine the coefficient N in Eq. (6). The displayed value, close to 5/3, indicates surface crystallization [28]

reliable conclusions with substantially smaller experimental effort [27]. We therefore studied a variant of Eq. (3) proposed by Matusita and Sakka [28]:

$$\ln\left(\frac{T_{c1}^2}{\beta}\right) = 1.052\frac{kE_c}{RT_{c1}} + constant, \quad (5)$$

where E_c is the corrected energy of crystallization, and k is a growth-dimensionality factor dependent on the crystallization mechanism. The exponent N of the heating rate on the left-hand side can be obtained from Ozawa's equation [29–31]:

$$\ln[-\ln(1-\alpha)] = -N\ln\beta + constant \quad (6)$$

Here α is the crystalline volume fraction, equal to ratio between the area under the portion of the peak truncated at temperature T and the total peak area, at the heating rate β. The slopes of the straight lines fitting the plots of $\ln[-\ln(1-\alpha)]$ versus $\ln\beta$ in Fig. 6b yield N=1.74±0.01.

Once N is determined, it is a simple matter to extract the activation energy on the right-hand side of Eq. (5) from the heating rates β and the measured T_{c1}. The crystallization activation energies obtained from this procedure, between 190 and 200 kJ/mol, are undistinguishable, within experimental error, from those obtained from the Kissinger expression without Matusita and Sakka's correction, Eq. (3). These energies compare favorably with the results reported in other non-isothermal analyses of crystallization [34].

Even more important than the activation energies is our result for the coefficient N. As explained in Ref. [33], the factor in the numerator of the first term on the right-hand side of Eq. (5) is $k=N-1$ for samples that underwent no heat treatment prior to thermal analysis. We conclude, therefore, that k=0.74, close to the fraction k=2/3 expected from surface nucleation [28, 32].

To highlight the importance of this conclusion, a cursory discussion of the physical origin of Eq. (6) seems warranted. Crystallization is initially limited only by the energy barriers separating the disordered phase from the ordered one. As time evolves, the crystallized fraction rises, and disordered material progressively becomes scarcer; crystallization then tends to slow down. Straightforward rate-equation analysis of this reduction yields the following relation between the crystallized-volume fraction $\alpha(t)$ resulting from thermal treatment at a fixed temperature T and the fraction $\alpha^*(t)$ that would have crystallized, had nucleation and growth been unconstrained:

$$\alpha(t) = 1 - \exp[-\alpha^*(t)]. \quad (7)$$

In Kolmogorov's interpretation, this equality expresses the probability that any small fraction of the glass will be crystallized after the time interval t [3]. For small t, Eq. (7) reduces to $\alpha(t)=\alpha^*(t)$. As $t\to\infty$, however, while $\alpha^*(t)$ grows without limit, the fraction $\alpha(t)$ asymptotically approaches 100 %.

The fraction $\alpha^*(t)$ depends on the nucleation rate I and the growth rate U at the temperature T, two quantities that in practice may be difficult to compute. To circumvent this difficulty, Avrami proposed the power law $\alpha^*(t)=C\ t^{\ n}$ to describe unconstrained crystallization [5–7], from which it follows that

$$\alpha(t) = 1 - \exp(-C\ t^n). \quad (8)$$

This expression can be alternatively written in the form

$$\ln[-\ln(1-\alpha)] = \ln(C) + n\ln(t), \quad (9)$$

which is the isothermal analogue of Eq. (6).

The exponent n in the second term on the right-hand side of Eq. (8) is therefore identified with the coefficient N found in our analysis of Eq. (6). To see how that number can help identify the source of crystallization, consider a fixed density N_S of nucleation centers on the surface of a growing volume of dimension $r(t)$. If a crystallite of relatively stable volume is rapidly formed around each of these centers, the initial growth of the crystallized fraction would be $\alpha^*(t)=h\ N_S\ r^2(t)$, where h is a dimensionless factor determined by the shape of the growing surface. If the dimension $r(t)$ grows at a fixed rate U, i.e., if $r(t)=U\ t$, then Eq. (7) reads

$$\alpha(t) = 1 - \exp\left(-hN_S U^2 t^2\right), \quad (10)$$

and comparison with Eq. (8) shows that $n=2$.

Other exponents point to other growth topologies. The result in Fig. 6b, N=1.74±0.01, indicated surface nucleation and led us to the microscopy laboratory in search of visual evidence to verify this finding.

Figure 7 shows optical microscopy (Fig. 7a) and AFM images (Fig. 7b–f) of the LBA matrix plates heated for 0, 1, and 5 h at 450 °C. Figure 7b–d show that, as one would expect from the previous discussion, the density of the crystalline phase rises as the thermal treatment time grows from t=0 (Fig. 7b) to t=5 h (Fig. 7d). A histogram inset at the bottom right-hand side of each panel shows the crystallite size distribution on the sample surface. The broad, askew distributions in Fig. 7c and d, and the evolution from the former to the latter suggest that we are here close to the source of nucleation.

The last two panels show mechanically thinned samples from the LBA matrix that was heat-treated for 5 h. The AFM images in Fig. 7e and f display the crystalline structure 510 μm and 1.02 mm, or 25 and 50 % of the original thickness, respectively, below the surface depicted in Fig. 7d. The 13 nm nanocrystals (average size) in Fig. 7e are substantially smaller than the 140 nm nanocrystals (approximate average size) in Fig. 7d. While the histogram in the latter panel describes a wide, irregular distribution, the

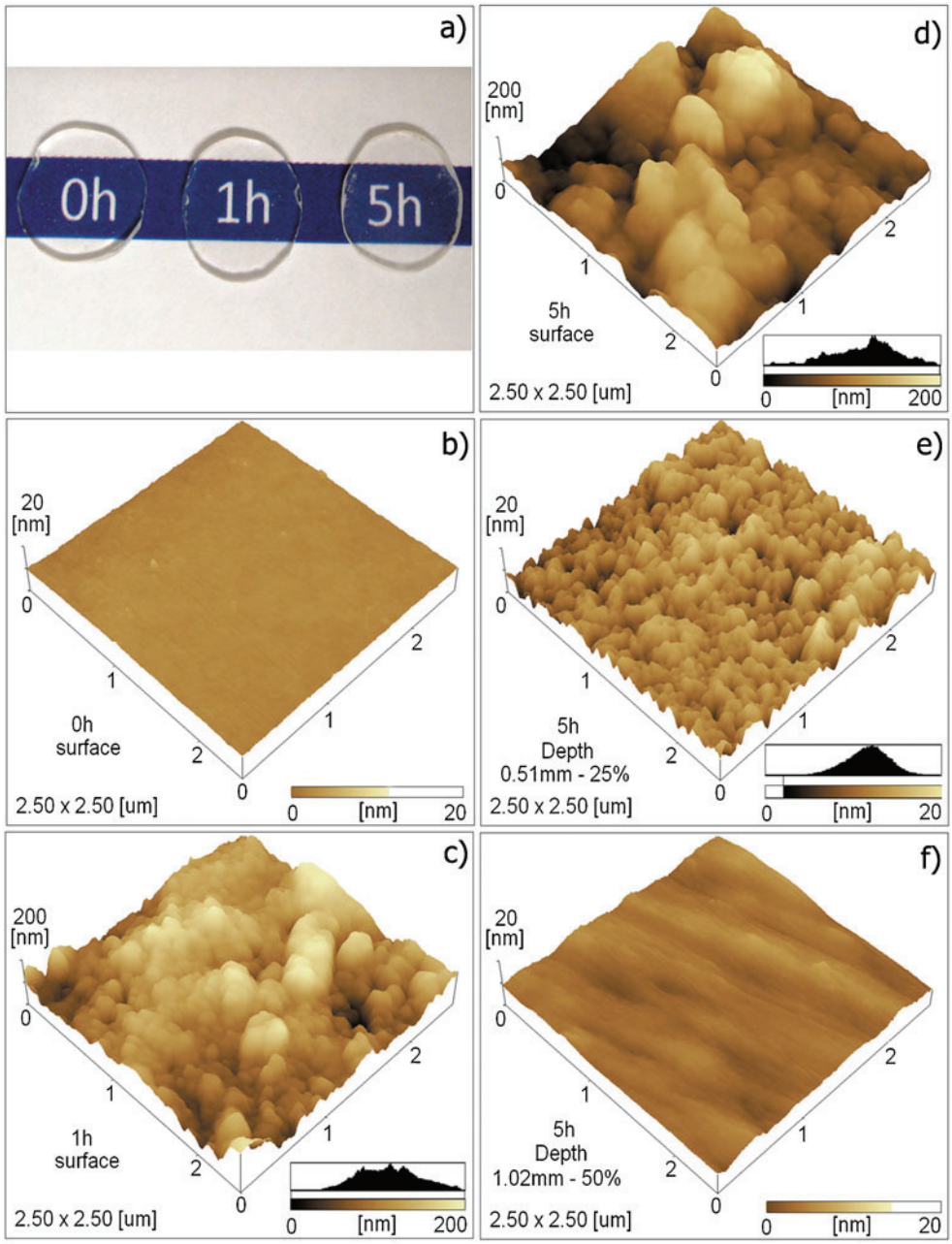

Fig 7 (*Color online*) **a** Optical microscopy and **b**–**f** AFM images of the LBA matrix. Panels **b**, **c**, and **d** show the surface of the matrix after 0, 1, and 5 h heat treatment, respectively, at 450 °C. Panels **e** and **f** show the surface of samples that were mechanically thinned to 75 and 50 % of the original thickness, respectively, after 5 h thermal treatment. The *inset* histograms in Panels **b**–**f** show the distribution of nanocrystal sizes on each surface. The distribution at the original surface after 5 h treatment [panel (**d**)] is wide, and the average crystal size is relatively large. Below the surface, at 510 μm depth [panel (**e**)] the distribution is more homogeneous and the crystallites, much smaller. At 1.02 mm depth [panel (**f**)], there is no sign of crystallization

histogram in the former displays a much narrower gaussian, and an average crystal size matching crystals grown in the highest crystal-lattice dimension, as in diopside [35] and silica [36] glasses, which grow first in the highest crystal-lattice dimension. The crystal sizes in Fig. 7c are in good agreement with the results of the Debye–Scherrer analysis depicted by open circles in Fig. 3, and the sizes in Fig. 7d, with the stars and open circles. Further below the surface, Fig. 7f shows no crystalline structure. The AFM results therefore confirm the conclusion drawn from Ozawa's expression, Eq. (6), that surface nucleation and growth constitute the dominant crystallization mechanism.

4 Conclusions

We have combined DTA with XRD, AFM, and theoretical considerations to provide an integrated description of crystal nucleation and growth in an LBA glass matrix. Differential thermal analysis, which probes thermally activated physical processes, including decomposition and post-melting sintering of the powder glass-forming composition, identified 450 °C with the onset of crystallization in the LBA matrix. Crystal growth at this temperature is sufficiently slow to allow quantitative control of crystallization. We computed crystallization activation energies with the Kissinger and the

more elaborate Matusita and Sakka equations and obtained similar results. Subsequent analysis of the experimental results on the basis of the procedure proposed by Ozawa indicated that crystallization starts at the surface, not in the bulk.

X-ray diffraction provided more detailed information on the structure of the crystallites. The diffractrograms revealed crystals with the $LiBO_2$ and $Li_3AlB_2O_6$ structures as well as a third, unidentified crystalline phase. Debye–Scherrer analysis of samples that had been thermally treated for time intervals varying from zero to 7 h revealed a competition between those phases during heat treatment.

AFM imaging determined average nanocrystal sizes in agreement with those resulting from the Debye–Scherrer analysis. The images revealed a distribution of crystallite sizes that becomes sharper and is shifted to smaller averages as one moves away from the surface into the glass matrix, fully confirming the central conclusion in this paper, that crystal growth in LBA glasses is nucleated at the surface.

Acknowledgments The authors would like to express their gratitude for financial support from the Brazilian agencies CNPq (especially 305373/2009-9 and 479799/2010-5 contracts), FAPEMIG, and CAPES.

References

1. V.M. Fokin, E.D. Zanotto, N.S. Yuritsyn, J.W.P. Schmelzer, J. Non-Cryst. Solids **352**, 2681–2714 (2006)
2. V.M. Fokin, M.L.F. Nascimento, E.D. Zanotto, J. Non-Cryst. Solids **351**, 789–794 (2005)
3. A. Kolmogorov, Izv. Akad. Nauk SSSR Ser. Mat. **1**, 355–359 (1937). in *Russian*
4. W.A. Johnson, R.F. Mehl, Trans. Am. Inst. Min. Metall. Pet. Eng. **135**, 416–443 (1939)
5. M. Avrami, J. Chem. Phys. **7**, 1103–1112 (1939)
6. M. Avrami, J. Chem. Phys. **8**, 212–224 (1940)
7. M. Avrami, J. Chem. Phys. **9**, 177–184 (1941)
8. B.V. Yerofyeyev, Dokl. Akad. Nauk USSR **52**, 511–514 (1946) (in *Russian*)
9. E. Osorio, O.D. Guterrez, C.G. Paucar, C.Z. Hadad, J. Lumin. **129**, 657–660 (2009)
10. S. Polosan, M. Secu, Rad. Meas. **45**, 409–411 (2010)
11. S. Watanabe, E.F. Chinaglia, M.L.F. Nascimento, M. Matsuoka, Rad. Prot. Dosimetry **65**, 79–82 (1996)
12. N.O. Dantas, E.O. Serqueira, M.J.V. Bell, V. Anjos, E.A. Carvalho, S.A. Lourenço, M.A. Pereira-da-Silva, J. Lumin. **131**, 1029–1036 (2011)
13. H. Inoue, K. Soga, A. Makishima, J. Non-Cryst. Solids **325**, 282–294 (2003)
14. A. Paul, R.W. Douglas, Phys. Chem. Glasses **6**(6), 212 (1965)
15. M. Srinivasa Reddy, G. Naga Raju, G. Nagarjuna, N. Veeraiah, J. Alloys Compd. **438**, 41 (2007)
16. P. Venkat Reddy, C.L. Kanth, V.P. Kumar, N. Veeraiah, P. Kistaiah, J. Non-Cryst. Solids **351**, 3752–3759 (2005)
17. L. Koudelka, P. Mosner, M. Zeyer, C. Jager, J. Non-Cryst. Solids **326**, 72 (2003)
18. I.W. Donald, B.L. Metcalfe, D.J. Bradley, M.J.C. Hill, J.L. McGrath, A.D. Bye, J. Mater. Sci. **29**, 6379 (1994)
19. Y.L. Yue, X.J. Yu, H.T. Wu, X.J. Chen, Mat. Res. Innovations **13**, 129 (2009)
20. E.B. Ferreira, M.L. Lima, E.D. Zanotto, J. Am. Ceram. Soc. **93**, 3757–3763 (2010)
21. A.S. Pedersen, N. Pryds, S. Linderoth, P.H. Larsen, J. KjØller, J. Thermal Anal. **64**, 887–894 (2001)
22. M. He, X.L. Chen, B.Q. Hu, T. Zhou, Y.P. Xu, T. Xu, J. Solid State Chem. **165**, 187–192 (2002)
23. M. Ohashi, H. Ogawa, A. Kan, E. Tanaka, J. Europ. Ceram. Soc. **25**, 2877–2881 (2005)
24. P. Scherrer, Nachrichten Gesell. Wiss. Göttingen **26**, 98–100 (1918)
25. P.F. Kerr, J.L. Kulp, Am. Mineral. **33**, 387 (1948)
26. H.E. Kissinger, J. Res. Natl. Bur. Stand. **57**, 217 (1956)
27. V.M. Fokin, A.A. Cabral, R.M.C.V. Reis, M.L.F. Nascimento, E.D. Zanotto, J. Non-Cryst. Solids. **356**, 358–36 (2010)
28. K. Matusita, S. Sakka, J. Non-Cryst. Solids **38&39**, 741–746 (1980)
29. N.P. Bansal, R.H. Doremus, A.J. Bruce, C.T. Moynihan, J. Am. Ceram. Soc. **66**, 233–238 (1983)
30. X.J. Xu, C.S. Ray, D.E. Day, J. Am. Ceram Soc. **74**, 909–9014 (1991)
31. C.S. Hsi, M.C. Wang, J. Mater. Res. **13**, 2655–2661 (1998)
32. D.W. Henderson, J. Thermal Anal. **15**, 325–331 (1979)
33. N. Syam Prasad, K.B.R. Varma, J. Am. Ceram. Soc. **88**, 357–361 (2005)
34. M.L.F. Nascimento, N.O. Dantas, Mater. Lett. **61**, 912–916 (2007)
35. M.L.F. Nascimento, E.B. Ferreira, E.D. Zanotto, J. Chem. Phys. **121**, 8924–8928 (2004)
36. M.L.F. Nascimento, E.D. Zanotto, Phys. Chem. Glasses **48**, 201–217 (2007)